remote sensing

MDPI

Article

Flood Hazard and Risk Assessment of Extreme Weather Events Using Synthetic Aperture Radar and Auxiliary Data: A Case Study

Esayas Gebremichael [1,*], Andrew L. Molthan [2], Jordan R. Bell [2], Lori A. Schultz [3] and Christopher Hain [2]

1 Department of Geological Sciences, Texas Christian University, 2955 South University Drive, Fort Worth, TX 76109, USA
2 Earth Science Branch, NASA Marshall Space Flight Center, Huntsville, AL 35805, USA; andrew.molthan@nasa.gov (A.L.M.); jordan.r.bell@nasa.gov (J.R.B.); christopher.hain@nasa.gov (C.H.)
3 Earth System Science Center, The University of Alabama in Huntsville, Huntsville, AL 35899, USA; lori.a.schultz@nasa.gov
* Correspondence: e.gebremichael@tcu.edu; Tel.: +1-817-257-4740

Received: 20 September 2020; Accepted: 29 October 2020; Published: 1 November 2020

Abstract: The Greater Houston metropolitan area has experienced recurring flooding events in the past two decades related to tropical cyclones and heavy inland rainfall. With the projected recurrence of severe weather events, an approach that outlines the susceptibility of different localities within the study area to potential floods based on analyses of the impacts from earlier events would be beneficial. We applied a novel C-band Sentinel-1 Synthetic Aperture Radar (SAR)-based flood detection method to map floodwater distribution following three recent severe weather events with the goal of identifying areas that are prone to future flood hazards. Attempts were made to calibrate and validate the C-band-based results and analyses to compensate for possible sources of error. These included qualitative and quantitative assessments on L-band aerial SAR data, as well as aerial imagery acquired after one of the events. The findings included the following: (1) most urban centers of Harris county, with few exceptions, are not believed to be prone to flooding hazards in contrast to the densely populated areas on the outskirts of Harris county; (2) nearly 44% of the mapped flood-prone areas lie within a 1 km distance of major drainage networks; (3) areas experiencing high subsidence rates have persistently experienced flooding, possibly exacerbated by morphological changes to the land surface induced by subsidence.

Keywords: Sentinel-1; coherence change detection (CCD); UAVSAR; flood hazard risk assessment

1. Introduction

Natural disasters arise from various natural processes and phenomena in the biosphere, lithosphere, hydrosphere, and atmosphere interacting and adversely affecting humans, infrastructure, and resources [1,2]. These events create hardship through loss of life and property, along with adverse impacts on agriculture through loss of yields [3,4]. In 2017, the United States incurred more than USD 306 billion of damage due to severe weather-induced disasters, including wildfires, hail, tornadoes, and flooding from extreme precipitation [5]. Flood damage from extreme precipitation following three severe weather events during the specified year (Hurricanes Harvey, Irma, and Maria) incurred the majority of this damage [5]. Several studies have shown that the frequency, intensity, and impact of natural disasters, especially flood hazards resulting from severe weather events, have increased over the years and are projected to increase in the coming decades, partly due to human-induced alterations to the environment and climate change [2,4,6–9]. Moreover, largely anthropogenic-led

activities, including extreme fluid withdrawal rates, have induced surface deformation processes that have modified the land surface and have further intensified the impact and extent of inundation following landfalling tropical cyclones and other coastal flood regimes, as the impact of storm surges is intensified by a rise in sea levels and further exacerbated by long-term high subsidence rates [10,11]. Furthermore, flooding in areas proximal to the courses of streams and rivers following severe weather events may be aggravated by the subsidence of flood control structures built along the courses of these streams and rivers [11–14]. Subsidence processes on such structures could alter the flow dynamics and enhance the spatial extent and depth of floodwaters [12,13].

1.1. Study Area

The study area encompassed part of the Greater Houston metropolitan area (surface area: 10,374 km^2; Figure 1). The area has experienced recurring and intense flooding events in the past two decades related to tropical cyclones and heavy inland rainfall. Some of the major events include Tropical Storm Allison (2001), the April 2016 North American storm complex sometimes referred to as the "Tax Day storm," Hurricane Harvey (2017), and Tropical Storm Imelda (2019). Hurricane Harvey was one of the wettest rainfall events in the history of the United States, producing an unprecedented amount of rainfall, estimated to be between 36 and 48 inches, in Houston and the surrounding areas from 25 to 31 August (2017). It resulted in severe flooding and associated damage amounting to USD 125 billion [15,16]. The second and less intensive recent flood event that affected the study area was the Tax Day storm (17–18 April 2016) that dumped more than 17 inches of rainfall over a short period of time and caused billions of dollars of flood damage [17,18]. Tropical Storm Imelda (18–21 September 2019) poured as much as 43 inches of rainfall (NOAA NCEI, 2020) into parts of southeast Texas, although the severity of the flooding event and the spatial/aerial coverage over the study area were not as significant and intense as the previous two flood events [19,20].

In addition to flooding resulting from extreme precipitation from hurricanes and cyclones over the study area, intense rainfall in the upstream watersheds of the San Jacinto and Brazos rivers that pass through the study area (Figure 1) further complicate the flooding problem [21]. Over time, urbanization and other intense anthropogenic activities across the study area have led to changes in the land cover and land surface elevation, which are believed to have aggravated the impacts of flooding [14,22,23]. [22] estimated that over the past two decades (1997–2017), nearly 2040 km^2 (±400 km^2) of land in the Greater Houston area has been changed to less permeable developed land cover, out of which 14% were wetland areas.

1.2. Floodwater Delineation Approaches and Possible Limitations

Remote sensing datasets complement in situ observations and modeling when investigating large-scale processes regarding the monitoring of hazards, specific disasters, and post-disaster response and recovery activities because of the wide spatial coverage and routine data acquisition capability [24,25]. Historically, datasets acquired by optical sensors, such as from Landsat and other coarse- to medium-resolution Earth observation missions, have been widely used for numerous natural hazard and disaster management and response studies, including flooding from hurricanes and cyclones [26–30]. Floodwater delineation studies utilizing datasets from optical sensors are mostly based on one of the three main techniques and approaches. The first, a fairly simple approach, is to discern flooded pixels through visual interpretation of multiband composite images [31]. The second and most widely utilized method is image classification algorithms based on the spectral properties of pixels in images retrieved by a single or combination of sensors or platforms (e.g., [32]). Classification of fused imagery from sensors of varying temporal and spatial resolution, such as Landsat and Moderate Resolution Imaging Spectroradiometer (MODIS), have also been used to map the impact of flood disasters from extreme precipitation [33]. Third, the analysis and interpretation of the derived indices from the multispectral satellite data, such as that of the Normalized Difference Water Index (NDWI), is another technique that is being used to detect inundations from floodwaters following extreme

weather conditions [34]. In all the above-stated studies, the prevalence of cloud conditions has been cited as a principal limitation for using such datasets to monitor the impacts during and following severe weather events. Heavy rainfall events include cloud cover as the rain falls and often lingering cloud cover post-event that obscures optical remote sensing. Night-time conditions lack the illumination necessary for land and water mapping using optical sensors and, hence, the effectiveness of these sensors during the hazard event and immediately following under such conditions is partly limited.

Synthetic Aperture Radar (SAR) remote sensing complements optical remote sensing approaches in natural hazard and disaster-related studies through active acquisition of Earth observations at day and at night and under widely varying weather conditions [35]. SAR sensors emit electromagnetic pulses and receive the signal returned from the surface, termed as backscatter, in the form of amplitude and phase. The amplitude component of the backscattered energy is a measure of the strength of the reflectance or reflectivity of the surface, while the phase is proportional to the distance between the sensor antenna and the ground target. The SAR backscatter signal from a target surface is dependent on several factors. These can be broadly classified as radar system properties (wavelength, polarization, etc.) and target surface properties (e.g., dielectric constant, the geometry of the target, and surface roughness) [36–39]. The launch of the European Space Agency (ESA) Sentinel-1 SAR satellite constellation has broadened disaster monitoring and response studies through the acquisition and free, open access distribution of high-resolution temporal (6–12 days) and spatial (5 m range × 20 m azimuth) wide-swath imagery of the Earth's surface [40,41]. Sentinel-1 SAR missions operate in the C-band wavelength (5.6 cm wavelength and 5.4 GHz frequency) and provide dual polarimetric data for a wide range of applications [42,43].

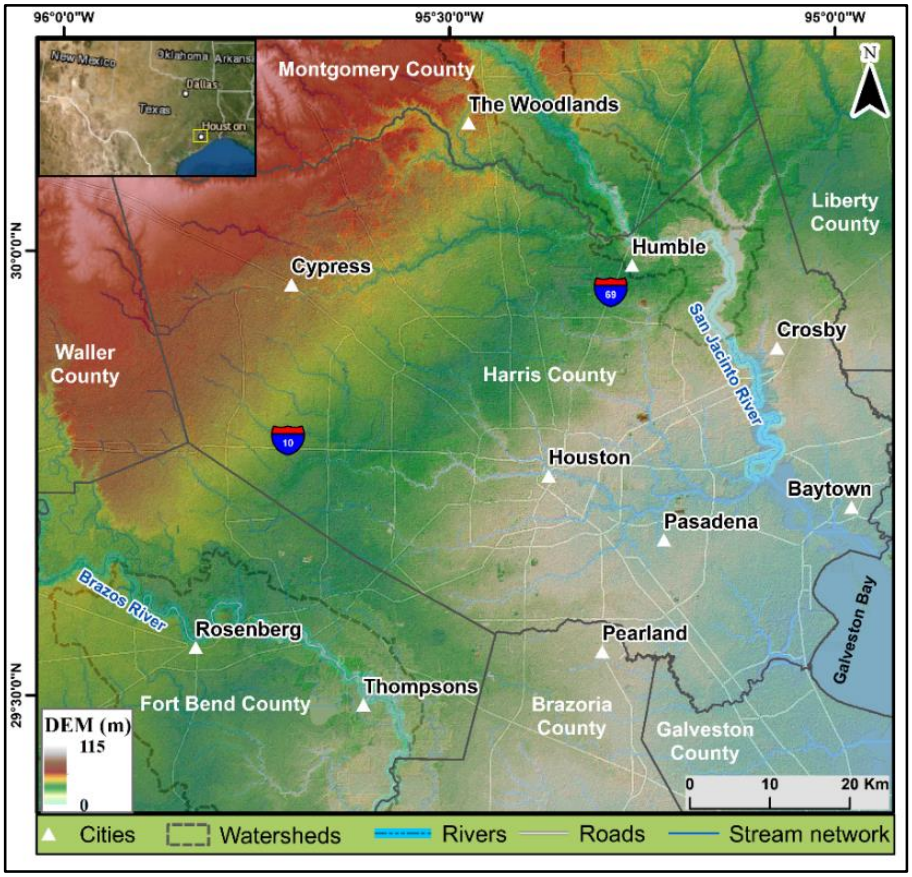

(**a**)

Figure 1. *Cont.*

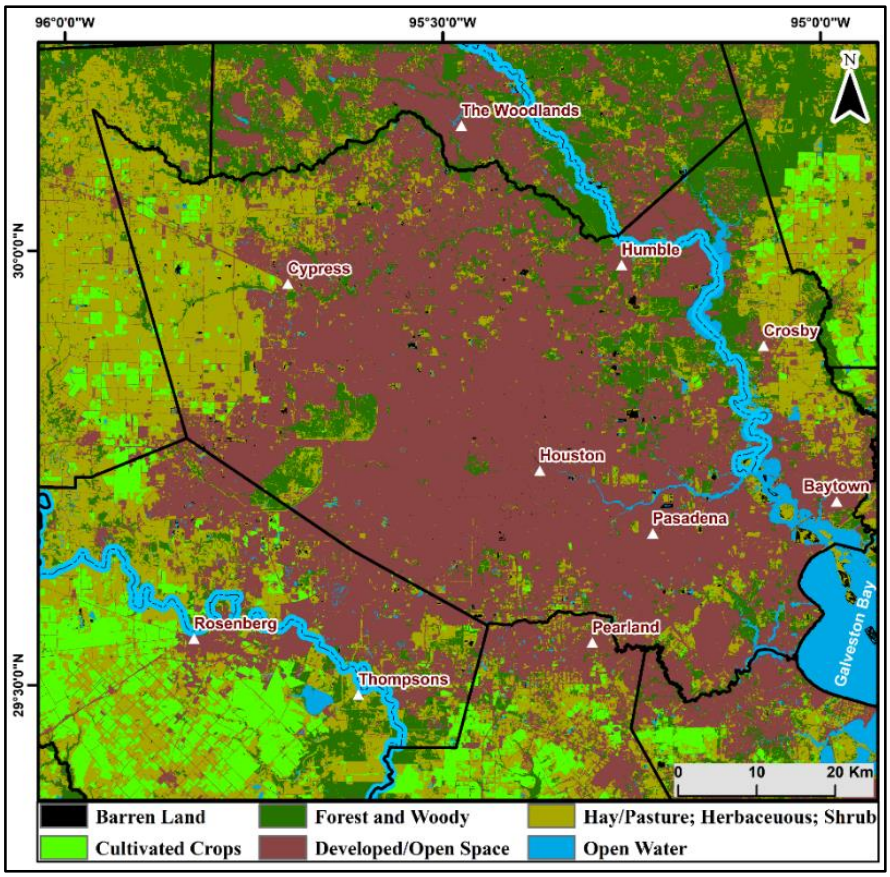

(**b**)

Figure 1. (**a**) The study area, including Houston city and parts of the surrounding areas (counties Harris, Fort Bend, Waller (partial), Montgomery (partial), Liberty (partial), Brazoria (partial), and Galveston (partial)). The two rivers (San Jacinto and Brazos) that cut through the northeastern and southwestern parts along with the respective watersheds (West Fork San Jacinto and Lower Brazos, respectively, shown with dotted black lines), and surface elevation data retrieved from a digital elevation model (DEM) are also shown. The inset shows the location of the study area in the USA. (**b**) Land cover distribution map derived from the National Land Cover Database (NLCD; [44]). The landcover classes were re-grouped into the six major dominant land cover types prevalent in the study area.

Several studies have relied on the analysis and interpretations of individual SAR datasets to assess the impacts of floods during and following extreme weather events. For instance, [45] used the manual thresholding approach on pre- and post-Hurricane Harvey Sentinel-1 SAR amplitude images to delineate flooded agricultural fields in Texas and Louisiana. They validated the SAR-based mapping using manually-derived ground reference validation data from the Landsat-7/8 and Sentinel-2 satellites. The wide time gap between the data acquisition of the two datasets (SAR and optical data) and the dense cloud cover conditions during the event makes it difficult to reliably assess the extent of floods in conjunction with the SAR data. Moreover, in the absence of validating data to support flooding beneath the vegetation cover due to the limited capability of the C-band signals from the Sentinel-1 mission to see beyond the top surface, mapping exercises might over/underestimate the extent of flooding [46,47]. However, this condition is dependent on several factors, including the crop/vegetation growth stage (e.g., leaf-on/leaf-off conditions), distribution (e.g., sparse forest and dense forest), and crop/vegetation type [48,49]. More importantly, the results and interpretations from single SAR scenes are complex, affected by various forms and sources of errors and factors that affect the backscatter signal that might impact the reliability of the derived products. For instance, SAR shadow zones or large paved and smooth surfaces, such as airport runways, might be erroneously mapped as flooded surfaces because

of their low backscatter values [50–53]. Change detection methods that highlight temporal changes in the property and reflectivity of the same area on the Earth's surface at different times observed using multiple SAR image acquisitions have proven to be more robust in detecting surface changes that have resulted from flooding hazards [37,54].

Two types of change detection methods are widely employed using SAR data to observe surface changes from flooding events: Amplitude (intensity) change detection (ACD) and coherent change detection (CCD) [55,56]. SAR datasets acquired before and after an event or series of events with similar geometry and mode of acquisition are used in both methods. The ACD method is based on changes in the intensity/amplitude values of the SAR backscatter signal, while the CCD method infers surface changes through observations of changes in interferometric coherence by taking both the amplitude and phase changes between image acquisitions into consideration [57]. A decline in the coherence value (or a complete decorrelation) is deemed to represent surface changes that have resulted from events and processes that disturbed or altered the arrangement of scatterers within a pixel [58–61]. Coherence-based change detections are more capable of and sensitive to detecting subtle surface changes that otherwise may not be noticeable in SAR amplitude images due to little changes and variations in backscattering intensity [47,60–62].

Numerous studies have examined land surface changes that have resulted from flooding events using change detection methods applied to SAR images and, in some instances, supported by relevant auxiliary data. [63] applied multi-temporal amplitude change assessment to pre- and post-event (flooding) high-resolution X-band (3.1 cm wavelength; [64]) images of the Italian COSMO-SkyMed constellation to delineate the extent of flooding in their study area caused by the landfall of Hurricane Harvey. They validated the SAR-based results using social media data and the hydraulic model. However, their analysis included the assumption that all water areas will have low backscatter, potentially excluding inundated areas with rough water surfaces resulting from different factors. For instance, changes in the roughness of water surfaces following heavy rainfall and windy conditions might alter the backscatter properties of the target surface and might lead to inaccurate interpretation [54]. Moreover, the developed approach did not consider temporal changes in the surface that could be revealed through interferometric approaches. For instance, the amplitude values of contrasted surfaces such as roads and urban areas, where there might be substantial anthropogenic-led land surface changes between acquisitions, may not reveal the changes in the properties of the target at different times. In the case of vegetation-covered areas, ACD-based floodwater mapping approaches might inaccurately classify the changes resulting from seasonal changes in the growth cycle of the vegetation as flooded pixels (beneath vegetation).

In a two-step approach, outlined by [50], to map flooding brought about by heavy rains from Hurricane Harvey within the urbanized area of Houston, double-bounce/bright features in SAR images were initially identified through multi-temporal SAR intensity analysis. This was followed by CCD assessment in search of a decline in coherence over the earlier identified features to map flooding. The presence of vegetation in the investigated area and the resulting decline in coherence between acquisitions has been cited as a possible reason for the underdetection of flooded areas [50]. While CCD approaches improve flood mapping by resolving the ambiguities posed by amplitude/intensity-based detections where coherence decline between acquisitions is principally used to map floods, caution must still be applied where surface changes from anthropogenic activities between acquisitions might result in a decrease in coherence and, hence, an inaccurate classification. As stated earlier, floodwater detection approaches based on data acquired by short wavelength sensors, such as C-band Sentinel-1 and X-band COSMO-SkyMed, could potentially underdetect floodwaters in vegetated areas. The flood mapping studies over the study area outlined above could potentially underdetect the spatial distribution of floodwaters due to this fact in the absence of data and approaches to validate the results. A comprehensive approach that integrates robust SAR data-based change detection assessment techniques with relevant datasets and methods could compensate for the

limitations stated earlier and could improve the accuracy of flood detections through the calibration or validation of existing models.

Many flood mapping studies undertaken over parts of the study area have focused on mapping the extent of the floods caused by Hurricane Harvey. With the projected recurrence of severe weather events and the expected disasters and their adverse implications, an approach that outlines the susceptibility of different localities within the study area to flooding based on assessment of the impacts from earlier events would be beneficial. In this study, an integrated approach using novel SAR-based techniques and ancillary datasets were developed to map land surface changes resulting from major flooding from periods of severe weather-induced heavy rainfall over the city of Houston and parts of the surrounding metro area. Such areas included portions or the entirety of the following counties: Harris, Fort Bend, Waller, Montgomery, Liberty, Brazoria, and Galveston (Figure 1). The ultimate goal of this study was to identify areas that are at a greater susceptibility of future severe weather-induced flooding so that appropriate mitigation efforts can be undertaken.

2. Materials and Methods

We used temporal changes in coherence as a measure of land surface changes that resulted from three severe weather events (i.e., Tax Day storm, Hurricane Harvey, and Tropical Storm Imelda) to map the spatial extent of the recurrently flood-impacted areas in Houston city and its surrounding areas.

Eleven descending Interferometric Wide Swath (IW) mode Single Look Complex (SLC) Sentinel-1A/B radar images acquired before and after the three investigated flood seasons (spanning from 14 March 2016 to 25 September 2019; Table 1) were used for the multitemporal CCD-based analyses. Four SAR images (three pre-event and one post-event) for each of the 2016 and 2017 flood events and three images (two pre-event and one post-event) for the recent (2019) flood event were used to generate the coherence products (Table 1). Although SAR imaging is capable of depicting surface conditions under varying weather conditions, intense precipitation can potentially create image distortions during heavy precipitation conditions caused by the attenuation of the SAR signal by rain cells [65]. As a result, SAR images in which attenuation attributed to intense rainfall has been noted over wide zones of the study area, characterized by a wide dark patch, were excluded from the data analysis. Result generation was facilitated through the Hybrid Pluggable Processing Pipeline (HyP3; [66])—a cloud-based platform of the Alaska Satellite Facility that uses GAMMA software to processes Sentinel-1 SLC data.

Table 1. Synthetic Aperture Radar (SAR) datasets used for mapping and validating the flood occurrences following severe weather events in the study area.

SAR Data Type		Flight Path	Perpendicular Baseline (m)	Temporal Baseline (Days)	Severe Weather Event
Sentinel-1A/B SLC Granule Pairs (yyyymmdd)	20160314–20160326	Descending	97.6625	12	Tax Day storm
	20160326–20160407	Descending	14.3211	12	
	20160407–20160419	Descending	–39.2588	12	
	20170812–20170818	Descending	–55.1226	6	Hurricane Harvey
	20170818–20170824	Descending	79.709	6	
	20170824–20170905	Descending	–20.2613	12	
	20190907–20190913	Descending	36.2323	6	Tropical Storm Imelda
	20190913–20190925	Descending	28.6556	12	
UAVSAR GRD Granules (yyyymmdd)	20170902 (Brazos_14938)	Descending			Hurricane Harvey
	20170902 (sanjac_14939)	Descending			

Note: GRD refers to ground range detected; SLC, Single Look Complex; UAVSAR, Uninhabited Aerial Vehicle Synthetic Aperture Radar.

The data processing steps for generating the coherence products include co-registration of the Sentinel-1 imagery using the matching and spectral diversity method, resampling the reference and

secondary scenes, generation of differential interferograms, and estimation of the interferometric coherence [67]. The final product is multilooked by a factor of 4 in azimuth and 20 in range, resulting in a spatial resolution of 80 m. Coherence (Υ), the amplitude of the complex correlation coefficient between SAR images A and B, is estimated using the following equation [68,69]:

$$\Upsilon = \left| \frac{\frac{1}{n}\sum_{i=0}^{n} A_i B_i^*}{\sqrt{\frac{1}{n}\sum_{i=0}^{n} A_i A_i^* \frac{1}{n}\sum_{i=0}^{n} B_i B_i^*}} \right| \quad (1)$$

where i represents individual pixels of images A and B, respectively; A^* and B^* are the complex conjugates of SAR images A and B, respectively; n signifies the number of neighboring pixels to be estimated [69]. The magnitude of Υ ranges from 0 to 1, signifying decorrelated to coherent image pairs, respectively. Coherence values vary as a function of the time span between SAR image acquisitions (termed temporal baseline), as well as the spatial (perpendicular) distance between two satellites (termed perpendicular or geometrical baseline), although the significance of these two variables is highly dependent on the wavelength of the SAR sensor and the surface changes [70,71].

We propose a methodology herein in which two sets of coherence products derived from the Sentinel-1A/B SLC datasets, termed hereafter as pre-event (Υ_b) and co-event (Υ_c), were analyzed to observe the temporal change in the coherence values of individual pixels before and after a flood event. The Υ_b represents the coherence product resulting from the analysis of the image pairs before the event, while Υ_c represents the coherence product resulting from the analysis of the image pairs before and after the event. Temporal changes in the pre-event coherence stack were assessed by applying a statistical approach: Retaining target pixels with coherence values in the range of one-third standard deviation (<0.03) from the mean coherence value of all of the pre-event coherence pixels, that is, a near-zero (absolute value) slope of the linear regression trend line (<0.02) over the investigated time interval. This is expected to preserve pixels with consistent values throughout all pre-event coherence products, ensuring that pixels whose values significantly declined in the co-event pairs represent areas impacted by flooding rather than other processes/events such as anthropogenic surface alterations and seasonal changes in vegetation phenology. Establishing pixels of stable coherence conditions is beneficial for identifying pixels of reduced coherence in the co-event products indicative of potential flooding. Therefore, a second set of coherence stack was generated using the co-event SAR image pairs. Individual pixels in the co-event coherence products were compared qualitatively and quantitatively with the final pre-event stable pixels to identify pixels where a significant decline in coherence with respect to the pre-event product (greater than 45% decrease in value) indicates a greater likelihood of surface change attributable to flooding (Υ_{final}). A sketch showing the workflow of the processing steps described above is shown in Figure 2. We tested the effectiveness of the devised approach to identify flood risk areas in Houston city and its surrounding areas using datasets from the first two flooding events (i.e., the Tax Day storm and Hurricane Harvey; Table 1). We then validated/extended the approach of detecting flood risk areas on datasets from the most recent flooding event (i.e., Tropical Storm Imelda; Table 1) in a bid to identify the recurrence of flooding over the areas mapped in the previous two flood events (Figures 3–5).

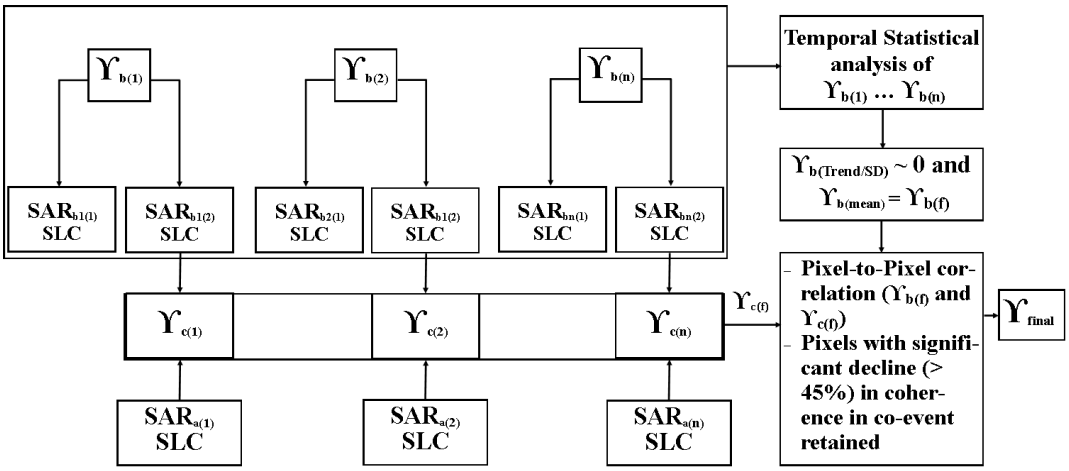

Figure 2. Flowchart portraying the procedures to map inundated areas using coherence change detection (CCD). $SAR_{bn(n)}$ and $SAR_{a(n)}$ refer to the pre- and post-disaster SAR images, respectively; $\Upsilon_{b(n)}$ and $\Upsilon_{c(n)}$ signify pre-disaster and co-event coherence products, respectively; $\Upsilon_{b(f)}$ and $\Upsilon_{c(f)}$ refer to the (final) products of the pre-event and co-event pairs, respectively; Υ_{final} denotes the resulting final coherence change product. SD denotes the standard deviation.

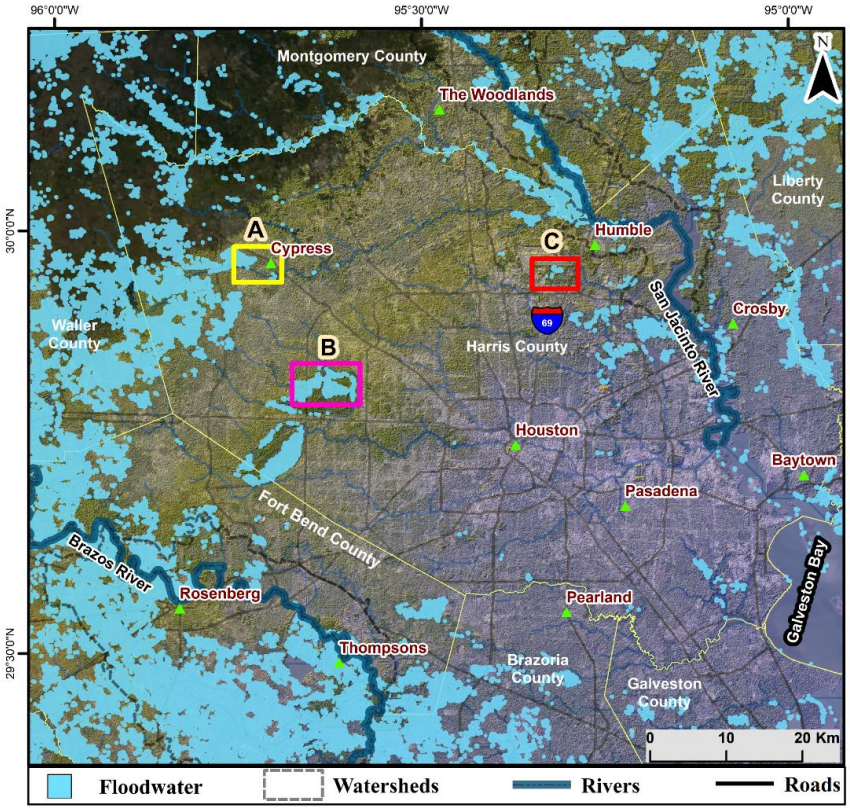

Figure 3. CCD-based map of the recurrently flood-affected areas of Houston and its surrounding areas, generated using Sentinel-1 data acquired before and after the flooding events following the Tax Day storm (2016) and Hurricane Harvey (2017). Three sites (**A**–**C** shown in yellow, pink, and red, respectively) were randomly selected to demonstrate the changes in the coherence of pixels, thereby signifying flooding.

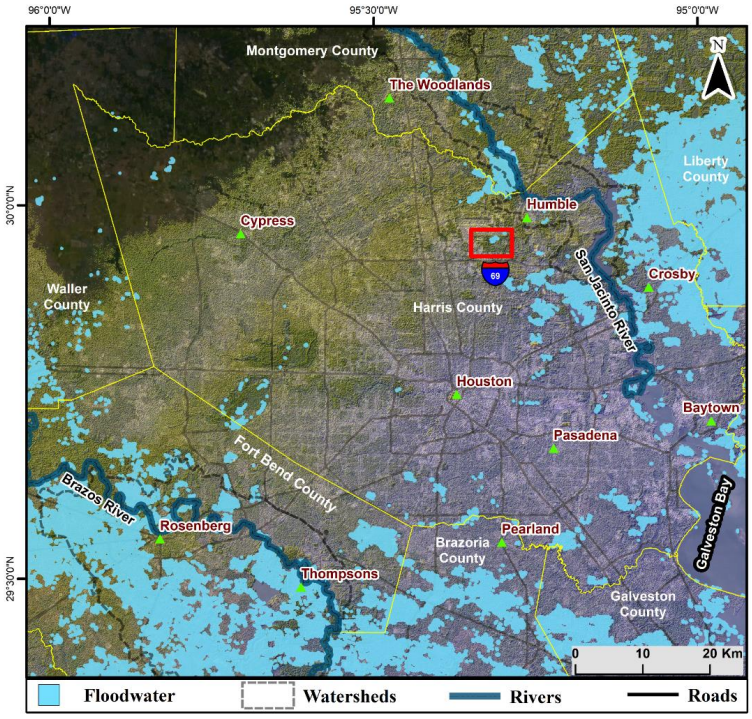

Figure 4. Flood mapping of Houston and its surrounding areas following Tropical Storm Imelda (2019) derived using Sentinel-1 data. The results demonstrate the reliability of the developed CCD-based approach for identifying the recurrently flood-affected areas of Houston and its surrounding areas using datasets from earlier severe weather events (i.e., Tax Day storm and Hurricane Harvey). The George Bush International Airport (red box) area was selected as a test site to demonstrate the change in coherence observed as a result of flooding following the three severe weather events.

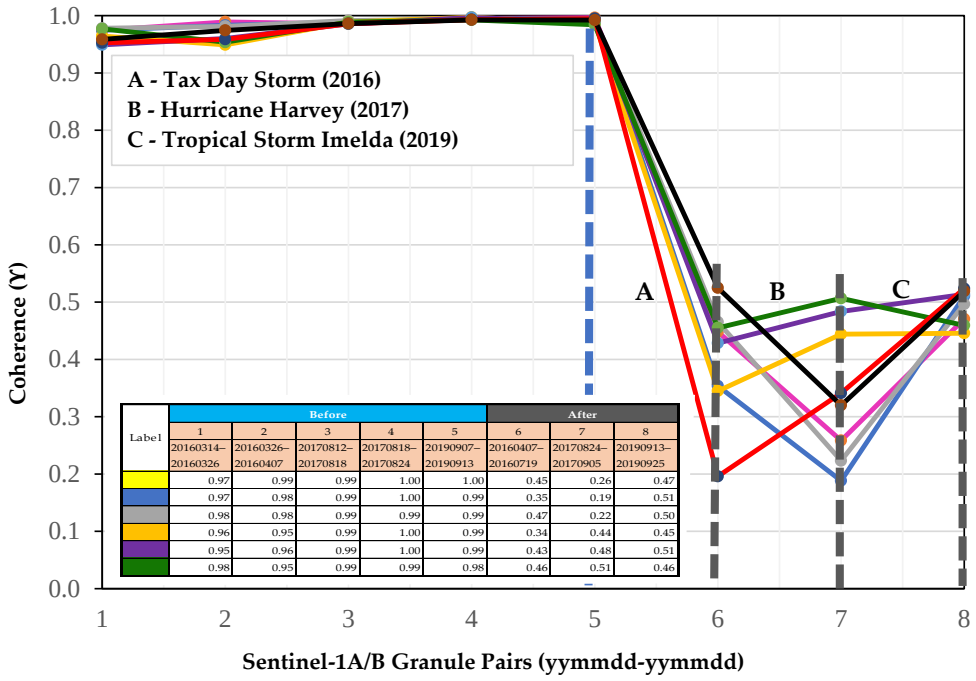

Label	Before					After		
	1	2	3	4	5	6	7	8
	20160314–20160326	20160326–20160407	20170812–20170818	20170818–20170824	20190907–20190913	20160407–20160719	20170824–20170905	20190913–20190925
	0.97	0.99	0.99	1.00	1.00	0.45	0.26	0.47
	0.97	0.98	0.99	1.00	0.99	0.35	0.19	0.51
	0.98	0.98	0.99	0.99	0.99	0.47	0.22	0.50
	0.96	0.95	0.99	1.00	0.99	0.34	0.44	0.45
	0.95	0.96	0.99	1.00	0.99	0.43	0.48	0.51
	0.98	0.95	0.99	0.99	0.98	0.46	0.51	0.46

Figure 5. Changes in the coherence values of the pixels in the George Bush Intercontinental Airport area (for location, see Figure 4). With few exceptions, Hurricane Harvey seems to have inflicted significant surface changes in the area, as revealed by the higher percentage of decline in coherence values (64.64%), followed by the Tax Day storm (58.96%) and then Tropical Storm Imelda (50.32%).

Moderate- to high-resolution topographic datasets that depict the variation in the morphology of the surface are critical inputs in flood models and simulations. In this study, further calibration of the SAR-derived flood mapping product was undertaken with the support of the moderate spatial resolution (12.5 m) Phased Array type L-band Synthetic Aperture Radar (PALSAR) Digital Elevation Model (DEM). The products derived from analyzing the DEM data, such as slope, flow direction, and watershed, and stream network delineation were incorporated into the SAR-based model to help reduce false detections by eliminating flood pixels from steep slopes, shadowed regions, or on the surface of existing water bodies [72].

Sections of the study area are covered with various types of vegetation with varying density and distribution (Figure 2). As a result, the quality of the proposed methodology that is based on the C-band Sentinel-1 dataset needs to be tested to see whether the approach is able to map the flood underneath dense vegetation, noting that coherence-based detections of flood occurrence will be challenging across scenes of varying seasons, especially if vegetation in the area experiences a strong annual growth cycle (e.g., crops versus slower-growing forest). Land cover products from the recent (2016) National Land Cover Database (NLCD) [44] were used to select woody and forested areas that could possibly limit the capability of the sensor to observe the land surface conditions beyond the top canopy/woody surfaces. We applied the polarimetric decomposition technique on targeted Uninhabited Aerial Vehicle Synthetic Aperture Radar (UAVSAR) datasets with flight paths adjacent to the San Jacinto River and Brazos rivers (Table 1) acquired post-Hurricane Harvey (2 September 2017) to classify/map inundation beneath the vegetation of three selected sites (Figure 6). We then attempted to qualitatively compare the findings with the C-band-based flood mapping approach. The UAVSAR mission acquires fully polarimetric L-band SAR data, flying from an altitude of 12.5 km and mapping a 20 km swath area [73]. We selected two densely vegetated areas located near the courses of the two major rivers to test the robustness of the proposed approach in detecting floods outside sparsely vegetated and urbanized areas (Figures 1b and 6). Data analysis and result generation, that is, flood detection, were performed using the quadrature polarization (quad-pol) ground range detected/projected (GRD) UAVSAR product as the input in PolSARpro software [74]. The key data processing steps included: (1) Deriving coherency matrix [T3] products from the input UAVSAR GRD files; (2) modeling/decomposing the coherency elements as a contribution of three-component scattering mechanisms—surface (termed "Odd") scattering, double-bounce (termed "Dbl") scattering, and volume (termed "Vol") scattering—using the Freeman–Durden polarimetric decomposition method [74–76]. An empirical threshold value of 0.5 was set to clearly distinguish the contribution of the three components. Odd scattering classification represents the return from open water bodies, while Vol represents scattering from the vegetation canopy. Dbl classification represents the return from corner reflectors and, in this case, it signifies the double-bounce between the vegetation stalk and the underlying water, indicating inundated vegetation [77,78].

A further attempt to qualitatively validate the accuracy and reliability of the proposed approach was undertaken through a spatial correlation assessment between the output of the flood detection analysis and the ground truth datasets acquired during the flood events. The ground truth datasets included the aerial imagery acquired by the NOAA Remote Sensing Division and the reports from the Federal Emergency Management Agency (FEMA).

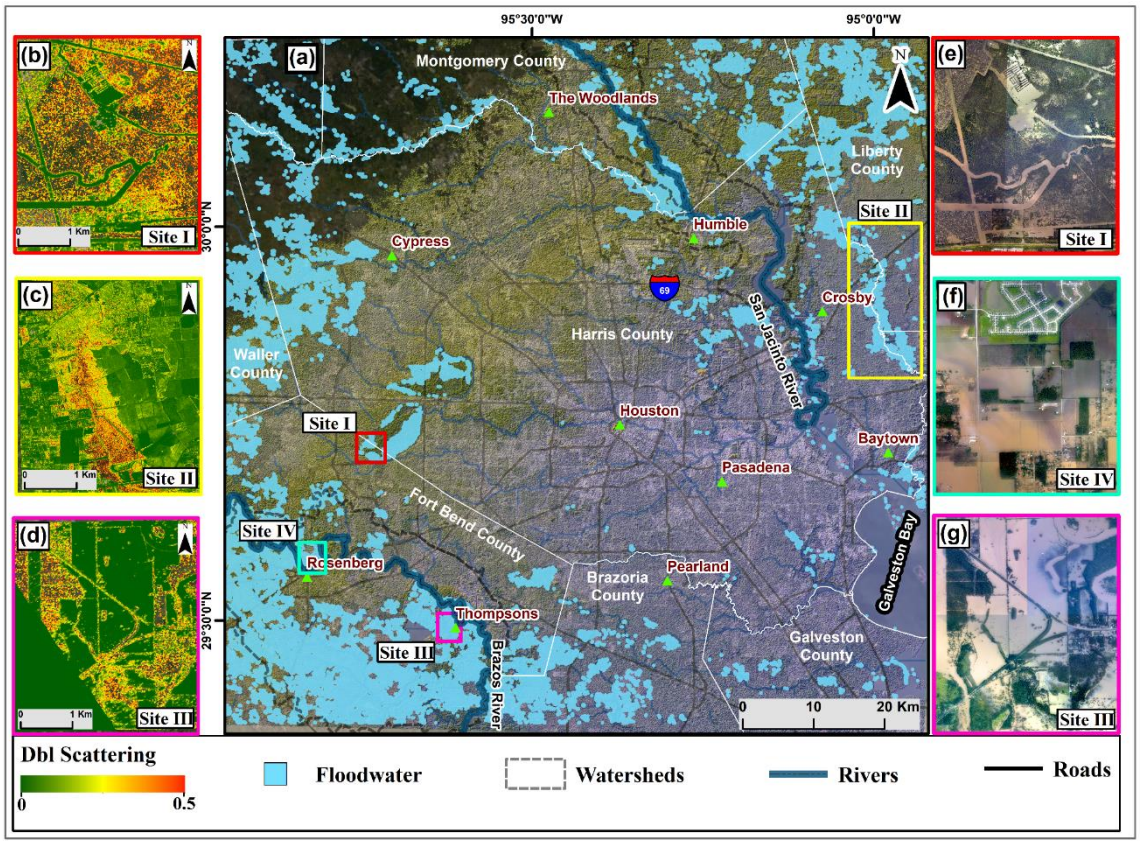

Figure 6. Validation of the Sentinel-1-based flood-prone areas using unsupervised classification applied to the Uninhabited Aerial Vehicle Synthetic Aperture Radar (UAVSAR) images (Figure 6a–d) and National Oceanic and Atmospheric Administration (NOAA) aerial photos acquired during Hurricane Harvey (Figure 6e–g). Four sites (Sites I–IV) in different parts of the study area were selected to demonstrate the reliability of the floodwater detection approach using Sentinel-1 data as the input. Two sites in which there is an overlap of UAVSAR and NOAA aerial image acquisitions (Sites I and III) were selected to correlate the flood mapping from the two sources and to further demonstrate the accuracy of the proposed approach.

3. Results

3.1. Sentinel-1 SAR-based Flood Mapping

Interferometric coherence change analyses were applied to 11 Sentinel-1 descending orbit SAR images to map sections of Houston city and its surrounding areas that have recurrently been affected by severe weather-induced flooding. The proposed approach to map flood risk areas was initially developed based on the analyses applied to Sentinel-1 datasets acquired before and after the Tax Day storm and Hurricane Harvey events (Table 1). The accuracy of the proposed model in identifying flood-prone areas was tested using Sentinel-1 datasets from the recent (2019) flood event over the study area induced by Tropical Storm Imelda (Table 1).

The following section is dedicated to analyzing the results of detecting and mapping floods over the study area in the earlier (2016 and 2017) flood events followed by the recent (2019) event. Moreover, attempts made to validate the Sentinel-1 SAR-based flood mapping method using different datasets and techniques are also discussed.

3.1.1. The Tax Day Storm and Hurricane Harvey Flood Events

The results of the analysis of SAR data to detect flood recurrence during the 2016 and 2017 flood events are shown in Figure 3. For the pre-event stack (Table 1), pixels that exhibited consistency in

values from the overall pre-event coherence stack (mean = 0.97; standard deviation = 0.013) were retained through the approach explained earlier. The approach retained 87% of the total pixels in the pre-event stack, and these pixels were compared against the co-event (20160407–20160419; 20170824–20170905; Table 1) coherence pixels to identify those pixels whose values had declined by more than 45%. The final flood map for the 2016–2017 flood event revealed that 7.5% of the total initial pixels (prior to the pre-event coherence analysis) and only 8.6% of the total pixels that exhibited coherence consistency were found to have lost their values by more than 45% when compared to the co-event stack. These pixels are presumed to represent areas that have repeatedly experienced severe weather-induced flooding and are assumed to be prone to the risk of flooding in possible future events. The two flood events recurrently impacted nearly 781 km^2 of land surface in the Greater Houston area (Figure 3). The predominantly inundated land cover types include forest and woody areas (28%), agricultural fields (25%), and herbaceous and shrub-covered areas (35%) (Figures 1b and 3). It should be noted that even though the dominant land cover types affected by the flood hazards in these areas are those listed earlier, there are pockets of land with developed land cover type along with dense population distribution within these areas. For instance, large swaths of land affected by flooding in Fort Bend county (population density >600 people/square mile [79]) are covered with crops, hay, shrub, and forest (Figures 1b and 3), yet patches of developed areas (Figures 1b and 3) inhabited by dense populations within and surrounding these areas were also impacted by the flooding.

The impact of the flood hazards is not uniform throughout the study area. Some of the areas that were widely impacted by the events include areas along the courses of the San Jacinto and Brazos rivers, the creeks in Houston and its surrounding areas, the Galveston Bay area, and large swaths of land to the northeast, southeast, and northwest of downtown Houston (Fort Bend, Waller, Harris, and Liberty counties, respectively; Figure 3). Assessment of the temporal changes in coherence in these areas revealed a decline in the coherence values that we attributed to changes that resulted from the severe weather-induced flooding. In the following section, the changes/decline in the coherence values in selected areas that represent various sections (and land cover types) of the study area, identified using the approach outlined above as being recurrently impacted by the two flood events, are discussed.

The Cypress Creek area of Houston (yellow box in Figure 3) has a documented history of flood recurrence [80] and the two flood events discussed herein also affected areas within and surrounding the creek. For instance, the mean pre-event coherence value of the pixels close to the banks of Cypress Creek (e.g., the outskirts of Cypress City in Harris county located 26 miles northwest of downtown Houston (yellow box in Figure 3)) amounted to 0.99; however, the 2016 and 2017 flood events prompted significant changes in the surface conditions, as noted by a substantial decline in the co-event coherence value (mean: 0.31). Similarly, the Bear Creek area (pink box in Figure 3) was also significantly impacted by the two flood events, as indicated by the substantial reduction in the coherence values of the pixels in the area following the events (mean pre-event coherence = 0.97; mean co-event coherence = 0.34). Two areas were selected here (black dotted lines in Figure 3) to demonstrate the impact of flooding in areas proximal to the two rivers in the study area. Extensive flooding has been noted in the Lower Brazos watershed (black dotted line near Brazos River in Figure 3), including the city of Rosenburg (Fort Bend county) and the wide agricultural fields lying proximal (on the bank) to the course of Brazos River (Figures 1b and 3). The pixels in this part of the study area exhibited more than a 61% decrease in coherence values compared to the values before the severe weather events (mean pre-event coherence = 0.96; mean post-event coherence = 0.38) that is attributed herein to the flooding events (Figure 3). Similarly, the outskirts of Humble, located along Interstate 69 within the West Fork San Jacinto watershed (black dotted line in the upstream part of San Jacinto River in Figure 3) and situated adjacent to the course of San Jacinto River, experienced recurrent flooding, as noted by the vast decline (up to 70%) in the coherence pixels following the two major events—although the impact is much more pronounced in the case of Hurricane Harvey than the 2016 Tax Day storm (mean pre-event coherence = 0.98; mean co-event coherence = 0.30). Given that parts of the study area, including the banks/proximal areas to the major rivers and the small creeks

and streams, are dominated by dense vegetation, an attempt to validate the CCD-based assessment was undertaken to ascertain whether the cause for the observed decline in coherence emanated from the surface changes attributed to flooding and not from other natural or anthropogenically driven alterations (discussed in Section 3.2). Recurrent flooding was noted in the northeastern part of the investigated area, including parts (south) of the George Bush Intercontinental Airport (shown in a red box in Figure 3; mean pre-event coherence = 0.98; mean co-event coherence = 0.40). Likewise, the pixels of the outskirts of Baytown city located near the Galveston Bay area (east of Houston city; Figure 3) also demonstrated a similar pattern of coherence decline (mean pre-event coherence = 0.96; mean post-event coherence = 0.38).

3.1.2. Tropical Storm Imelda Flood Event

The reliability of the developed model, based on temporal coherence change assessments of Sentinel-1 imagery as a measure of surface changes for mapping the recurrence of flood impact on the Greater Houston area, was tested on the two earlier flood events: Tax Day storm and Hurricane Harvey. The flooding that arose as a result of the recent (2019) severe weather event, Tropical Storm Imelda, was used as a validation event to test the robustness of the proposed approach to map areas that are at greater risk of flooding following possible severe weather events. Prior to the assessment of the impact following Tropical Storm Imelda (co-event analysis), the consistency of the pre-event coherence pixels identified in the earlier two severe weather events was tested using the approach outlined in Section 2. The results of the analysis of SAR data to detect flood recurrence following Tropical Storm Imelda are shown in Figure 4. As outlined earlier, the intensity and coverage of the flooding event as a result of the heavy rains from Tropical Storm Imelda are much smaller compared to the earlier flood events, and hence, the potential risk of flooding in parts of the study area identified through the datasets from the earlier two severe weather events could not be fully corroborated. Our analyses showed that the impact of the storm, and hence the extent of flooding, was severe in the southwestern (Fort Bend county; Figure 4), south (Brazoria and Galveston counties; Figure 4), and northeastern (Harris and Liberty counties; Figure 4) parts of the study area. Similar to the earlier severe weather-induced flooding events, the areas proximal to the two major rivers (San Jacinto and Brazos rivers) also experienced large-scale flooding following the recent event (Figure 4). In general, the pattern and extent of flooding for the areas affected by Tropical Storm Imelda highly resemble the pattern and extent of floodwater distribution observed in the earlier events (Figures 3 and 4). Figure 5 shows a demonstration of the flood recurrence in the George Bush Intercontinental Airport area (red box in Figure 4) in all three of the severe weather events using the temporal change in coherence values. As revealed in Figure 5, the three events induced a significant decline in the coherence of the pixels/surfaces located in the airport area. All in all, our analysis shows that more than 71% of the delineated pixels that exhibited a significant decline in coherence values following Tropical Storm Imelda lie at (same position) or within a 500 m radius of the pixels mapped using the same approach for the earlier events. One possible reason for this slight offset between pixels might be due to possible co-registration errors among the Sentinel-1 pairs during data analysis; nonetheless, the assessment demonstrated the reliability of the proposed approach to map areas that are at risk of being inundated by flooding from probable future severe weather events using Sentinel-1 datasets acquired before and after Tropical Storm Imelda.

3.2. Validation

3.2.1. UAVSAR Data Classification

Sentinel-1 satellites and C-band SAR sensors are limited in their ability to penetrate the vegetation canopy to sample the underlying structure of the vegetation and surface. To validate flood detections and to develop an understanding of C-band capabilities, L-band UAVSAR datasets from Hurricane Harvey were used to compare the C- and L-band observations and to refine the flood detections derived based on Sentinel-1 datasets. Unsupervised classifications based on the Freeman–Durden Polarimetric

decomposition [76] of the UAVSAR acquisitions for Hurricane Harvey were analyzed to validate the detected floodwaters beneath dense vegetation/canopy covers using the Sentinel-1 based datasets and techniques. Two fully polarimetric UAVSAR images adjacent to the courses of the San Jacinto and Brazos rivers and their surrounding areas were selected (Table 1) because of the prevalence of various forms of dense vegetation cover, as noted on the NLCD 2016 product (Figure 1b). Figure 6 shows a comparison of the results of the UAVSAR-based classification and Sentinel-1-derived flood detection for three localities in the study area. Sites I (George Bush Park area), II (Cedar Bayou Woods area), and III (near Thompsons city) are covered with a wide variety of sparse-to-dense vegetation (Figure 1b) with a wood and canopy structure that might limit the penetration depth of the C-band signals.

The unsupervised classification of the L-band UAVSAR imagery revealed that high values (>0.2) for the Dbl compared to the Odd and Vol components were observed for the selected sites, denoting the presence of floodwaters within and on the outskirts of the vegetated areas. For instance, the polarimetric classification of Thompsons city (Figure 6d) that lies along the course of Brazos River distinctly classified water from Brazos River (near-zero Dbl scattering) from the floodwater beneath vegetation, as demonstrated by high Dbl scattering values (>0.2). Similarly, we analyzed the spatial correlation between the floodwater pixels detected using the CCD- and UAVSAR-based approaches for Site II (Figure 6) after resampling the UAVSAR classification product to the resolution of the CCD product. The analysis showed that close to 62% of the pixels classified by the UAVSAR as flooded (Dbl > 0.2) were detected by the Sentinel-1 based floodwater detection approach. The fact that the UAVSAR classification is based on data acquisition following a single event, while the CCD-based assessment is generated using datasets from two events, could be a plausible reason for the moderate level of correlation observed between the two results. The discrepancy in spatial resolution between the products even though resampling was carried out could have also led to a slight offset between the pixels, thereby reducing the spatial correlation between the products. Potential errors or ambiguity emanating either from the acquisition and calibration of the UAVSAR data [81] or from the misclassification of pixels [82] could have contributed to the observed moderate correlation with the C-band SAR result. A qualitative comparison of the Sentinel-1-derived results with the L-band UAVSAR-based method in the selected sites is shown in Figure 6a–d. In general, the C-band-based flood detection method (for inundated vegetation) largely corresponds well with the L-band UAVSAR-based detection in all of the selected sites (Figure 6a–d), indicating the effectiveness of the developed method for identifying floodwaters, even in the presence of dense-to-sparse vegetation cover over the surface.

3.2.2. NOAA Aerial Imagery

Following Hurricane Harvey, the NOAA Remote Sensing Division acquired aerial imagery (30 August–2 September 2017) of the selected sites in the study area [83]. Even though cloud cover partly obscured the clarity of the images over some parts of the study area, they provided a vivid representation of the ground conditions (spatial resolution ranging from 35 to 50 cm [83]) during the severe weather event. We visually compared the images acquired by NOAA to the SAR-derived (Sentinel-1 and UAVSAR) flood detection over three localities in the study area (Figure 6a,e–g). In two of these sites (Sites I and III; Figure 6), covered with dense forest and woody land cover types (Figure 1b), there was an overlap in image acquisition by both the UAVSAR and NOAA missions (maximum gap of one day between image acquisitions). As can be seen in Figure 6, the results of the flood detection based on the two data sources spatially correlated well. Moreover, the floodwaters detected using the two (UAVSAR and NOAA aerial imagery) datasets also correlated well with the flood detection based on the approach using the Sentinel-1 datasets. Site IV (Figure 6) is largely covered with cultivated crops, and to demonstrate the potential of the Sentinel-1-based approach to detect floodwater in similar land cover types, a comparison between the NOAA imagery and the Sentinel-1 data-based flood mapping was undertaken (Figure 6a,f). Similar to the case of the forest and woody land cover types, the proposed floodwater detection based on the Sentinel-1 data was also able to capture the floodwater in such land cover types, as seen in Figure 6f. By and large, the NOAA images correlated well with the

SAR-derived flood detection, further confirming the accuracy and reliability of the C-band SAR-based floodwater detection approach.

4. Discussion

Using the CCD technique applied to Sentinel-1 SAR datasets, we mapped Houston city and its surrounding areas that are vulnerable to flooding from possible future severe weather events. To offset the possible limitations of C-band SAR in detecting floodwaters underneath vegetation and to validate the accuracy of the adopted method, L-band data-based unsupervised classification of the UAVSAR data from Hurricane Harvey was undertaken. The quality and reliability of the SAR data-based product was further tested using the NOAA aerial imagery acquired during Hurricane Harvey. Although the validation of Sentinel-1-based flood mapping was based on datasets from a single severe weather event (i.e., Hurricane Harvey), the notion behind the validation exercise was to show the reliability of Sentinel-1-based floodwater detection in similar situations. Our analysis to identify areas that are susceptible to future floods based on past flood occurrences showed that most of the urban centers of the city of Houston, with the exception of a few localities (e.g., Bear Creek area; Figures 3, 4 and 6), are not believed to be impacted by recurrent flooding hazards that are persistent (standing water) and significant (spatially) enough to be detected by SAR remote sensors and validated through other data-gathering approaches. However, the disparity in the rate and intensity of the rainfall from the severe weather events, along with the other factors outlined above, might affect the delineation of the flood-prone areas described in this assessment. On the other hand, the major urban centers surrounding Harris county (e.g., Fort Bend and Galveston counties) have experienced recurrent floods and are highly susceptible to flood hazards (Figures 3, 4 and 6).

Furthermore, our findings showed that stream networks (Figures 3, 4 and 6) have a significant contribution to constraining the impact of flooding following severe weather events. The assessment report by FEMA (Mitigation Assessment Team Report [84]) on the impacts of Hurricane Harvey supports our evaluation of the role and significance of stream networks in controlling the spatial distribution of floodwaters in Harris county [84]. Overall, our assessment revealed that nearly 44% of the flood-prone areas mapped in all of the events lie within a 1 km radius of the drainage networks of the study area, including along the two major rivers in the northeastern and southwestern areas (Figures 3, 4 and 6). With the projected population increases and the accelerated anthropogenic land use/land cover (LULC) alterations in the counties (i.e., Harris, Fort Bend, and Montgomery counties) dissected by these two rivers [85,86], the impact from riverine flooding from future events could potentially be greater in the absence of proper mitigation efforts.

Land subsidence has been credited for aggravating the impact of flooding following severe weather events in parts of the study area [14,87]. For instance, the Galveston Bay area (Figure 1) has a history of being affected by recurrent flooding from the floodwaters of freshwater (San Jacinto River) following major severe weather events or tidal sources [14,87,88]. Land subsidence attributed to anthropogenic-led processes, such as high fluid extraction rates, has reportedly modified the slope and direction of flow, further exacerbating the problem [89,90]. Using the method discussed earlier, our assessment showed that parts of the coastal Galveston Bay area (e.g., city of Baytown) have repeatedly been affected by severe weather-induced flooding (Figure 3). Several studies have estimated higher rates of subsidence for the Galveston Bay area, including Baytown city and its surrounding areas (>5 mm/year; [14,91]). Large sections of these areas lie at a relatively lower elevation (<5 m; Figure 1) and if the current extreme utilization of resources continues unabated, the subsidence rate is expected to increase throughout the 21st century [14] and this, in turn, could potentially obliterate flood control structures in coastal areas and near inland waterbodies [92]. The impact of subsidence on aggravating floodwater distribution is much more pronounced in coastal areas. The combined effects of severe weather-induced storm surges, subsidence, LULC changes, high tides from tidal forcings, and rises in sea levels can influence the extent of flooding resulting from future landfalling

tropical cyclones and other coastal flood regimes, and could incur serious damage to communities and resources in coastal and near-coastal areas.

The impact of subsidence on increasing threat of flooding is not limited to coastal areas alone. Low-lying areas proximal to the floodplains of San Jacinto River in the upstream areas experiencing high subsidence rates [91,93] were identified in this study as being prone to flooding hazards from severe weather events (Figures 3 and 4). The impact is particularly enhanced in the lowland areas, such as near Crosby city and its surrounding areas (elevation <10 m; Figure 7) located along the course of San Jacinto River and bordering (south of) the West Fork San Jacinto watershed (Figure 7). Subsidence rates as high as 20–25 mm/year have been detected in these areas based on historical groundwater decline rates and recent Global Positioning System (GPS) data [93]. In this case, there was a subtle change in elevation gradient from the banks of San Jacinto River outward, heading inland, as shown in Figure 7. Similar to the notion stated earlier, moderate-to-high subsidence rates could change the elevation and orientation of the land surface of the river banks and the gradient of flow during flooding events, potentially affecting wider areas beyond the floodplain boundaries.

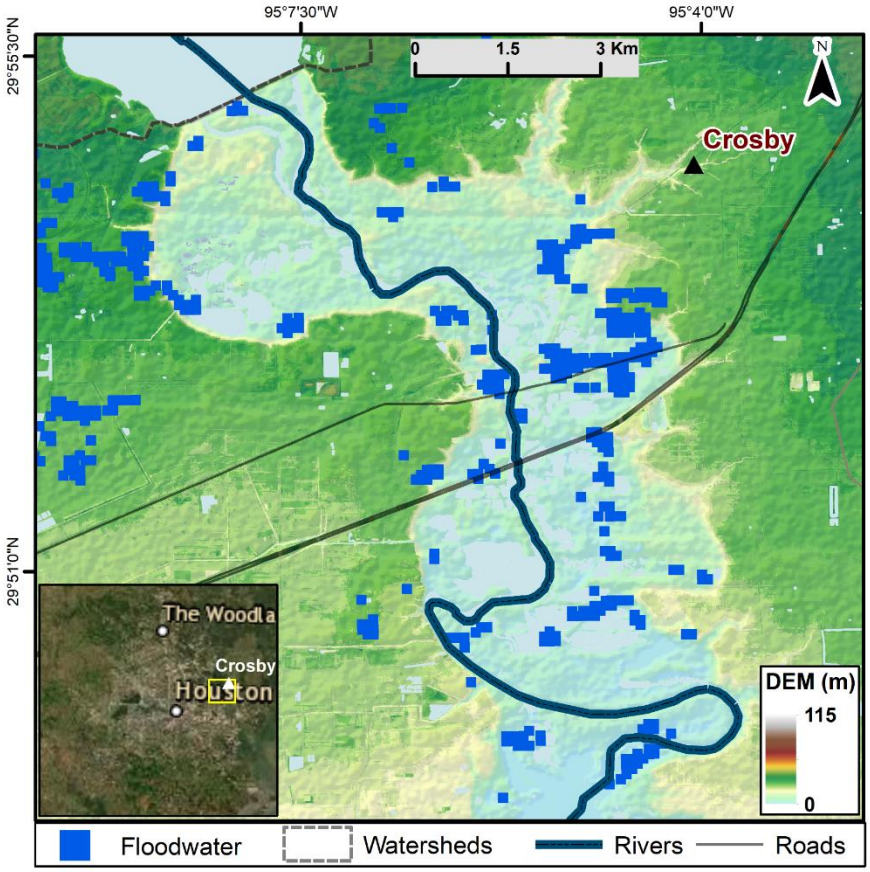

Figure 7. Flooding along the course of the San Jacinto River, particularly affecting the low-lying areas proximal to the course of the flow.

In summary, the projected rise in sea levels coupled with the land subsidence processes and increasing anthropogenic alterations to the land surface in the coastal areas, and similar processes and activities excluding the rise in sea levels in the inland areas, are expected to exponentially increase the vulnerability of communities and resources in the study area to flooding in the absence of robust resource management and flood resilience and protection strategies. Future works will concentrate on in-depth analysis of the nexus between the rise in sea levels, subsidence processes, and LULC changes in constraining the spatial extent of storm surge flooding in the coastal areas of the project site. Subsidence rates derived from interferometric SAR (InSAR) and calibrated with

ground-based observations will be integrated with elevation data, flood-induced changes detected by SAR, optical imagery, and other relevant datasets to assess the interconnection and significance of these processes on the overall distribution of flooding from storm surges following extreme weather events.

Although the approach managed to identify areas that are prone to flood hazards, a number of possible factors and uncertainties could potentially have led to over/underestimation of the extent of the impacted and flood-prone areas. One factor is the possible delay in the time that the Sentinel-1 satellite passed over the affected area. In the event of such a delay, the ground (flood) conditions might have changed by the time of the satellite overpass and thus the SAR image may not truly reflect the surface conditions that resulted from the event. For instance, Sentinel-1 passed over the study area following Hurricane Harvey on 5 September, even though the Hurricane concluded on 31 August, and this gap between the event and the SAR acquisition could have missed capturing the standing floodwaters that dissipated by the time of the satellite overpass. Second, the high cut-off empirical value (>45%) set in this study to identify pixels that exhibited a significant decline in coherence with the aim of weeding out false flood detections could have underestimated the spatial extent of the areas that are prone to flood hazards. The geometry and arrangement of the objects and structures in urban areas create a strong backscatter of SAR signals, even in the absence of floodwater on the surface, and, hence, change detection assessments with high threshold values as in the present study may not detect moderate-to-subtle changes in these areas. In addition, the data analysis procedures applied in this study, such as multilooking, that are intended to reduce the inherent noise on SAR signals partly degraded the resolution of the final product (final ground pixel resolution of 80 m), and thus moderate-scale flooded pixels might not have been captured in the final result.

5. Conclusions

In this study, we introduced a CCD-based approach that aims to delineate areas that are vulnerable to future flooding from severe weather events by analyzing the impact and recurrence of floods based on datasets from past events. The approach retains pre-event pixels that demonstrate consistent coherence properties (values) throughout all of the pre-event coherence products. These pixels are then compared with their corresponding pixels in the co-event coherence stack. Pixels that experienced a decline in coherence value of the threshold value of 45% or above are judged to indicate a greater likelihood of surface change attributable to flooding. The proposed approach was used to investigate areas in the Greater Houston region that are susceptible to potential future flooding based on datasets from three severe weather events that resulted in extensive flooding over the region. The quality and robustness of the proposed approach was tested and calibrated using a variety of auxiliary datasets. The possible factors that exacerbate the impact and distribution of floodwaters were also discussed. The approach and quality products generated and demonstrated in the research will help improve current floodwater detection and impact analysis techniques. Moreover, the proposed approach demonstrated critical data processing and analysis techniques that can be replicated in areas with similar settings to develop effective flood monitoring and early-warning systems.

Author Contributions: Conceptualization, E.G. and A.L.M.; methodology, E.G., A.L.M., and J.R.B.; software, E.G.; validation, E.G., A.L.M., and J.R.B.; formal analysis, E.G., A.L.M., J.R.B., L.A.S., and C.H.; writing—original draft preparation, E.G. and A.L.M.; writing—review and editing, E.G., A.L.M., J.R.B., L.A.S., and C.H. All authors have read and agreed to the published version of the manuscript.

Funding: This research received no external funding.

Acknowledgments: The authors would like to thank the Alaska Satellite Facility (ASF) for allowing them to use the Hybrid Pluggable Processing Pipeline (HyP3) cloud processing service for this research.

Conflicts of Interest: The authors declare no conflict of interest.

References

1. Hunter, L.M. Migration and Environmental Hazards. *Popul. Environ.* **2005**, *26*, 273–302. [CrossRef] [PubMed]
2. UNISDR. Terminology on Disaster Risk Reduction. 2009. Available online: https://www.unisdr.org/files/12659_UNISDRevaluation2009finalreport.pdf (accessed on 18 August 2020).
3. Motha, R.P. The Impact of Extreme Weather Events on Agriculture in the United States. In *Challenges and Opportunities in Agrometeorology*; Springer Science and Business Media LLC: Berlin/Heidelberg, Germany, 2011; pp. 397–407.
4. Powell, J.; Reinhard, S. Measuring the effects of extreme weather events on yields. *Weather. Clim. Extremes* **2016**, *12*, 69–79. [CrossRef]
5. NOAA NCEI. Billion-Dollar Weather & Climate Disasters 1980–2020. 2020. Available online: https://www.ncdc.noaa.gov/billions/events.pdf (accessed on 18 August 2020).
6. Bouwer, L.M. Have Disaster Losses Increased Due to Anthropogenic Climate Change? *Bull. Am. Meteorol. Soc.* **2011**, *92*, 39–46. [CrossRef]
7. Emanuel, K. Assessing the present and future probability of Hurricane Harvey's rainfall. *Proc. Natl. Acad. Sci. USA* **2017**, *114*, 12681–12684. [CrossRef] [PubMed]
8. Guerriero, L.; Ruzza, G.; Calcaterra, D.; Di Martire, D.; Guadagno, F.M.; Revellino, P. Modelling Prospective Flood Hazard in a Changing Climate, Benevento Province, Southern Italy. *Water* **2020**, *12*, 2405. [CrossRef]
9. USGCRP. Impacts, Risks, and Adaptation in the United States: Fourth National Climate Assessment, Volume II: Report-in-Brief. In Fourth National Climate Assessment. 2018. Available online: https://nca2018.globalchange.gov/chapter/24/ (accessed on 26 August 2020).
10. Fiaschi, S.; Tessitore, S.; Bonì, R.; Di Martire, D.; Achilli, V.; Borgstrom, S.; Ibrahim, A.; Floris, M.; Meisina, C.; Ramondini, M. From ERS-1/2 to Sentinel-1: Two decades of subsidence monitored through A-DInSAR techniques in the Ravenna area (Italy). *GISci. Remote Sens.* **2017**, *54*, 305–328. [CrossRef]
11. Yang, Z.; Wang, T.; Leung, R.; Hibbard, K.; Janetos, T.; Kraucunas, I.P.; Rice, J.; Preston, B.L.; Wilbanks, T. A modeling study of coastal inundation induced by storm surge, sea-level rise, and subsidence in the Gulf of Mexico. *Nat. Hazards* **2014**, *71*, 1771–1794. [CrossRef]
12. Abidin, H.Z.; Andreas, H.; Gumilar, I.; Wibowo, I.R.R. On correlation between urban development, land subsidence and flooding phenomena in Jakarta. *Proc. Int. Assoc. Hydrol. Sci.* **2015**, *370*, 15–20. [CrossRef]
13. Eggleston, J.; Pope, J.P. Land subsidence and relative sea-level rise in the southern Chesapeake Bay region. *Circular* **2013**, *1392*, 30. [CrossRef]
14. Miller, M.M.; Shirzaei, M. Land subsidence in Houston correlated with flooding from Hurricane Harvey. *Remote Sens. Environ.* **2019**, *225*, 368–378. [CrossRef]
15. Blake, E.S.; Zelinsky, D.A. National Hurricane Center Tropical Cyclone Report. Hurricane Harvey. AL092017. 2018. Available online: https://www.nhc.noaa.gov/data/tcr/AL092017_Harvey.pdf (accessed on 26 August 2020).
16. Risser, M.D.; Wehner, M.F. Attributable Human-Induced Changes in the Likelihood and Magnitude of the Observed Extreme Precipitation during Hurricane Harvey. *Geophys. Res. Lett.* **2017**, *44*. [CrossRef]
17. Collins, T.W.; Grineski, S.E.; Chakraborty, J.; Flores, A.B. Environmental injustice and Hurricane Harvey: A household-level study of socially disparate flood exposures in Greater Houston, Texas, USA. *Environ. Res.* **2019**, *179*, 108772. [CrossRef] [PubMed]
18. Kimmelman, M. Lessons from Hurricane Harvey: Houston's Struggle is America's Tale. *New York Times* 2017. Available online: https://www.nytimes.com/interactive/2017/11/11/climate/houston-flooding-climate.html (accessed on 26 August 2020).
19. Lozano, J.A. No Severe Impacts from Imelda as It Moves through Texas. 2019. Available online: https://apnews.com/8bd488fd53b54f979763e8929f8d3070 (accessed on 18 September 2020).
20. Pasch, R.J.; Roberts, D.P.; Blake, E.S. The 2019 Atlantic Hurricane Season: An Active and Destructive Year. *Weatherwise* **2020**, *73*, 32–39. [CrossRef]
21. Burnett, J. *Flash Floods in Texas*; Texas A&M University Press: College Station, TX, USA, 2008. [CrossRef]
22. Hakkenberg, C.; Dannenberg, M.; Song, C.; Ensor, K. Characterizing multi-decadal, annual land cover change dynamics in Houston, TX based on automated classification of Landsat imagery. *Int. J. Remote Sens.* **2018**, *40*, 693–718. [CrossRef]

23. Zhang, W.; Villarini, G.; Vecchi, G.A.; Smith, J.A. Urbanization exacerbated the rainfall and flooding caused by hurricane Harvey in Houston. *Nat. Cell Biol.* **2018**, *563*, 384–388. [CrossRef]
24. Joyce, K.E.; Wright, K.C.; Samsonov, S.V.; Ambrosia, V.G. Remote sensing and the disaster management cycle. In *Advances in Geoscience and Remote Sensing*; IntechOpen: London, UK, 2009; pp. 317–346.
25. Zhang, F.; Zhu, X.; Liu, D. Blending MODIS and Landsat images for urban flood mapping. *Int. J. Remote Sens.* **2014**, *35*, 3237–3253. [CrossRef]
26. Bell, J.; Molthan, A. Evaluation of approaches to identifying hail damage to crop vegetation using satellite imagery. *J. Oper. Meteorol.* **2016**, *4*, 142–159. [CrossRef]
27. Bell, J.R.; Gebremichael, E.; Molthan, A.L.; Schultz, L.A.; Meyer, F.J.; Hain, C.R.; Shrestha, S.; Payne, K.C. Complementing Optical Remote Sensing with Synthetic Aperture Radar Observations of Hail Damage Swaths to Agricultural Crops in the Central United States. *J. Appl. Meteorol. Clim.* **2020**, *59*, 665–685. [CrossRef]
28. Goffi, A.; Stroppiana, D.; Brivio, P.A.; Bordogna, G.; Boschetti, M. Towards an automated approach to map flooded areas from Sentinel-2 MSI data and soft integration of water spectral features. *Int. J. Appl. Earth Obs. GeoInf.* **2020**, *84*, 101951. [CrossRef]
29. Jedlovec, G.J.; Nair, U.; Haines, S.L. Detection of Storm Damage Tracks with EOS Data. *Weather Forecast.* **2006**, *21*, 249–267. [CrossRef]
30. Molthan, A.L.; Jedlovec, G.; Carcione, B. NASA satellite data assist in tornado damage assessments. *EOS* **2011**, *92*, 337–339. [CrossRef]
31. Notti, D.; Giordan, D.; Caló, F.; Pepe, A.; Zucca, F.; Galve, J.P. Potential and Limitations of Open Satellite Data for Flood Mapping. *Remote. Sens.* **2018**, *10*, 1673. [CrossRef]
32. Peng, B.; Meng, Z.; Huang, Q.; Wang, C. Patch Similarity Convolutional Neural Network for Urban Flood Extent Mapping Using Bi-Temporal Satellite Multispectral Imagery. *Remote Sens.* **2019**, *11*, 2492. [CrossRef]
33. Dao, P.D.; Liou, Y.-A.; Chou, C.-W. Detection of flood inundation regions with Landsat/MODIS synthetic data. In Proceedings of the International Symposium on Remote Sensing, Tainan, Taiwan, 22–24 April 2015.
34. Chignell, S.M.; Anderson, R.S.; Evangelista, P.; Laituri, M.; Merritt, D.M. Multi-Temporal Independent Component Analysis and Landsat 8 for Delineating Maximum Extent of the 2013 Colorado Front Range Flood. *Remote Sens.* **2015**, *7*, 9822–9843. [CrossRef]
35. Bouaraba, A.; Younsi, A.; Aissa, A.B.; Acheroy, M.; Milisavljević, N.; Closson, D. Robust techniques for coherent change detection using cosmo-skymed SAR images. *Prog. Electromagn. Res. M* **2012**, *22*, 219–232. [CrossRef]
36. Barrett, B.W.; Dwyer, E.; Whelan, P. Soil Moisture Retrieval from Active Spaceborne Microwave Observations: An Evaluation of Current Techniques. *Remote Sens.* **2009**, *1*, 210–242. [CrossRef]
37. Pulvirenti, L.; Chini, M.; Pierdicca, N.; Boni, G. Use of SAR Data for Detecting Floodwater in Urban and Agricultural Areas: The Role of the Interferometric Coherence. *IEEE Trans. Geosci. Remote Sens.* **2016**, *54*, 1532–1544. [CrossRef]
38. Toselli, F. *Applications of Remote Sensing to Agrometeorology: Proceedings of a Course Held at the Joint Research Centre of the Commission of the European Communities in the Framework of the Ispra-Courses, Ispra, Varese, Italy, 6–10 April 1987*; Springer Science & Business Media: Berlin/Heidelberg, Germany, 2013.
39. Walker, J.P.; Houser, P.R.; Willgoose, G.R. Active microwave remote sensing for soil moisture measurement: A field evaluation using ERS-2. *Hydrol. Process.* **2004**, *18*, 1975–1997. [CrossRef]
40. Lu, C.-H.; Ni, C.-F.; Chang, C.-P.; Yen, J.-Y.; Chuang, R.Y. Coherence Difference Analysis of Sentinel-1 SAR Interferogram to Identify Earthquake-Induced Disasters in Urban Areas. *Remote Sens.* **2018**, *10*, 1318. [CrossRef]
41. Vreugdenhil, M.; Wagner, W.; Bauer-Marschallinger, B.; Pfeil, I.; Teubner, I.; Rudiger, C.; Strauss, P. Sensitivity of Sentinel-1 Backscatter to Vegetation Dynamics: An Austrian Case Study. *Remote Sens.* **2018**, *10*, 1396. [CrossRef]
42. Tsyganskaya, V.; Martinis, S.; Marzahn, P.; Ludwig, R. Detection of Temporary Flooded Vegetation Using Sentinel-1 Time Series Data. *Remote Sens.* **2018**, *10*, 1286. [CrossRef]
43. Zin, W.W.; Kawasaki, A.; Takeuchi, W.; San, Z.M.L.T.; Htun, K.Z.; Aye, T.H.; Win, S. Flood Hazard Assessment of Bago River Basin, Myanmar. *J. Disaster Res.* **2018**, *13*, 14–21. [CrossRef]

44. Yang, L.; Jin, S.; Danielson, P.; Homer, C.; Gass, L.; Bender, S.M.; Case, A.; Costello, C.; Dewitz, J.; Fry, J.; et al. A new generation of the United States National Land Cover Database: Requirements, research priorities, design, and implementation strategies. *ISPRS J. Photogramm. Remote Sens.* **2018**, *146*, 108–123. [CrossRef]
45. Boryan, C.G.; Yang, Z.; Sandborn, A.; Willis, P.; Haack, B. Operational Agricultural Flood Monitoring with Sentinel-1 Synthetic Aperture Radar. In Proceedings of the IGARSS 2018—2018 IEEE International Geoscience and Remote Sensing Symposium, Valencia, Spain, 22–27 July 2018; pp. 5831–5834.
46. Oon, A.; Ngo, K.D.; Azhar, R.; Ashton-Butt, A.; Lechner, A.M.; Azhar, B. Assessment of ALOS-2 PALSAR-2L-band and Sentinel-1 C-band SAR backscatter for discriminating between large-scale oil palm plantations and smallholdings on tropical peatlands. *Remote Sens. Appl. Soc. Environ.* **2019**, *13*, 183–190. [CrossRef]
47. Refice, A.; Capolongo, D.; Pasquariello, G.; DaAddabbo, A.; Bovenga, F.; Nutricato, R.; Lovergine, F.P.; Pietranera, L. SAR and InSAR for Flood Monitoring: Examples With COSMO-SkyMed Data. *IEEE J. Sel. Top. Appl. Earth Obs. Remote Sens.* **2014**, *7*, 2711–2722. [CrossRef]
48. El Hajj, M.; Baghdadi, N.; Bazzi, H.; Zribi, M. Penetration Analysis of SAR Signals in the C and L Bands for Wheat, Maize, and Grasslands. *Remote Sens.* **2019**, *11*, 31. [CrossRef]
49. Plank, S.; Jüssi, M.; Martinis, S.; Twele, A. Mapping of flooded vegetation by means of polarimetric Sentinel-1 and ALOS-2/PALSAR-2 imagery. *Int. J. Remote Sens.* **2017**, *38*, 3831–3850. [CrossRef]
50. Chini, M.; Hostache, R.; Pelich, R.; Matgen, P.; Pulvirenti, L.; Pierdicca, N. Probabilistic Urban Flood Mapping Using SAR Data. In Proceedings of the IGARSS 2019—2019 IEEE International Geoscience and Remote Sensing Symposium, Yokohama, Japan, 28 July–2 August 2019; pp. 4643–4645.
51. Dasgupta, A.; Grimaldi, S.; Ramsankaran, R.; Pauwels, V.R.N.; Walker, J.P.; Chini, M.; Hostache, R.; Matgen, P. Flood Mapping Using Synthetic Aperture Radar Sensors From Local to Global Scales. In *Geomagnetically Induced Currents from the Sun to the Power Grid*; Wiley: Hoboken, NJ, USA, 2018; pp. 55–77.
52. Giustarini, L.; Hostache, R.; Matgen, P.; Schumann, G.J.-P.; Bates, P.D.; Mason, D.C. A Change Detection Approach to Flood Mapping in Urban Areas Using TerraSAR-X. *IEEE Trans. Geosci. Remote Sens.* **2013**, *51*, 2417–2430. [CrossRef]
53. Veljanovski, T.; Lamovec, P.; Pehani, P.; Oštir, K. Comparison of three techniques for detection of flooded areas on ENVISAT and RADARSAT-2 satellite images. In *Gi4DM 2011—GeoInformation for Disaster Management*; Springer: Berlin/Heidelberg, Germany, 2011.
54. Clement, M.; Kilsby, C.; Moore, P. Multi-temporal synthetic aperture radar flood mapping using change detection. *J. Flood Risk Manag.* **2018**, *11*, 152–168. [CrossRef]
55. Nico, G.; Pappalepore, M.; Pasquariello, G.; Refice, A.; Samarelli, S. Comparison of SAR amplitude vs. coherence flood detection methods—A GIS application. *Int. J. Remote Sens.* **2000**, *21*, 1619–1631. [CrossRef]
56. Sanyal, J.; Lu, X.X. Application of Remote Sensing in Flood Management with Special Reference to Monsoon Asia: A Review. *Nat. Hazards* **2004**, *33*, 283–301. [CrossRef]
57. Abdelfattah, R.; Nicolás, J. Interferometric Synthetic Aperture Radar Coherence Histogram Analysis for Land Cover Classification. In Proceedings of the 2006 2nd International Conference on Information & Communication Technologies, Damascus, Syria, 24–28 April 2006; Volume 1, pp. 343–348.
58. De Macedo, K.A.C.; Shiroma, G.H.X.; Wimmer, C.; Moreira, J.R.; Bradar, S.A.; De Macedo, K.A.C. Monitoring under foliage with airborne SAR. In Proceedings of the 2015 IEEE Radar Conference, Arlington, VA, USA, 10–15 May 2015; pp. 499–503.
59. Newey, M.; Barber, J.; Benitz, G.; Kogon, S. False alarm mitigation techniques for SAR CCD. In Proceedings of the 2013 IEEE Radar Conference (RadarCon13), Ottawa, ON, Canada, 29 April–3 May 2013; pp. 1–6.
60. Oishi, N.; Tsuchida, M.; Wakayama, T.; Hasegawa, H.; Okada, Y. A coherence improvement technique for coherent change detection in SAR interferometry. In Proceedings of the 2009 European Radar Conference (EuRAD), Rome, Italy, 30 September–2 October 2009; pp. 278–281.
61. Scheuchl, B.; Ullmann, T.; Koudogbo, F. Change detection using high resolution Terrasar-X data preliminary results. *Int. Arch. Photogramm Remote Sens. Spat. Inf. Sci.* **2009**, *38*, 5–10. Available online: http://www.isprs.org/proceedings/xxxviii/1_4_7-W5/paper/Scheuchl-185.pdf (accessed on 2 September 2020).
62. Al-Sharif, A.A.A.; Pradhan, B.; Hadi, S.J.; Mola, N. *Revisiting Methods and Potentials of SAR Change Detection*; Lecture Notes in Engineering and Computer Science, 3 LNECS; Newswood Limited: Hong Kong, China, 2013; pp. 2231–2237.

63. Scotti, V.; Giannini, M.; Cioffi, F. Enhanced flood mapping using synthetic aperture radar (SAR) images, hydraulic modelling, and social media: A case study of Hurricane Harvey (Houston, TX). *J. Flood Risk Manag.* **2020**, e12647. [CrossRef]
64. Chen, F.; Masini, N.; Yang, R.; Milillo, P.; Feng, D.; Lasaponara, R. A Space View of Radar Archaeological Marks: First Applications of COSMO-SkyMed X-Band Data. *Remote Sens.* **2015**, *7*, 24–50. [CrossRef]
65. Danklmayer, A.; Chandra, M. Precipitation induced signatures in SAR images. In Proceedings of the European Conference on Antennas and Propagation, EuCAP 2009, Berlin, Germany, 23–27 March 2009; pp. 3433–3437.
66. Hogenson, K.; Arko, S.A.; Buechler, B.; Hogenson, R.; Herrmann, J.; Geiger, A. *Hybrid Pluggable Processing Pipeline (HyP3): A Cloud-Based Infrastructure for Generic Processing of SAR Data*; AGU Fall Meeting Abstracts; American Geophysical Union: Washington, DC, USA, 2016.
67. Wegmuller, U.; Santoro, M.; Werner, C.; Cartus, O. On the Estimation and Interpretation of Sentinel-1 TOPS InSAR Coherence. In Proceedings of the Fringe 2015: Advances in the Science and Applications of SAR Interferometry and Sentinel-1 InSAR Workshop, Frascati, Italy, 23–27 March 2015. [CrossRef]
68. Just, D.; Bamler, R. Phase statistics of interferograms with applications to synthetic aperture radar. *Appl. Opt.* **1994**, *33*, 4361–4368. [CrossRef]
69. Washaya, P.; Balz, T.; Mohamadi, B. Coherence Change-Detection with Sentinel-1 for Natural and Anthropogenic Disaster Monitoring in Urban Areas. *Remote Sens.* **2018**, *10*, 1026. [CrossRef]
70. Kim, S.-W.; Wdowinski, S.; Amelung, F.; Dixon, T.H.; Won, J.-S. Interferometric Coherence Analysis of the Everglades Wetlands, South Florida. *IEEE Trans. Geosci. Remote Sens.* **2013**, *51*, 5210–5224. [CrossRef]
71. Wei, M.; Sandwell, D. Decorrelation of L-Band and C-Band Interferometry over Vegetated Areas in California. *IEEE Trans. Geosci. Remote Sens.* **2010**, *48*, 2942–2952. [CrossRef]
72. Ruzza, G.; Guerriero, L.; Grelle, G.; Guadagno, F.M.; Revellino, P. Multi-Method Tracking of Monsoon Floods Using Sentinel-1 Imagery. *Water* **2019**, *11*, 2289. [CrossRef]
73. Fore, A.G.; Chapman, B.D.; Hawkins, B.P.; Hensley, S.; Jones, C.E.; Michel, T.R.; Muellerschoen, R.J. UAVSAR Polarimetric Calibration. *IEEE Trans. Geosci. Remote Sens.* **2015**, *53*, 3481–3491. [CrossRef]
74. Pottier, E.; Ferro-Famil, L.; Allain, S.; Cloude, S.; Hajnsek, I.; Papathanassiou, K.; Moreira, A.; Williams, M.; Minchella, A.; LaValle, M.; et al. Overview of the PolSARpro V4.0 software. The open source toolbox for polarimetric and interferometric polarimetric SAR data processing. In Proceedings of the 2009 IEEE International Geoscience and Remote Sensing Symposium, Cape Town, South Africa, 12–17 July 2009; Volume 4, p. IV-936. [CrossRef]
75. An, W.; Lin, M. A Reflection Symmetry Approximation of Multilook Polarimetric SAR Data and its Application to Freeman–Durden Decomposition. *IEEE Trans. Geosci. Remote Sens.* **2019**, *57*, 3649–3660. [CrossRef]
76. Freeman, A.; Durden, S.L. *Three-Component Scattering Model to Describe Polarimetric SAR Data*; San Diego '92; SPIE: Washington, DC, USA, 1993; Volume 1748, pp. 213–224. [CrossRef]
77. Alijani, G.; Hasanlou, M.; Azizi, Z. Classifying UAVSAR Polarimetric Synthetic Aperture Radar (PolSAR) Imagery Using Target Decomposition Features. *Multidiscip. Digit. Publ. Inst. Proc.* **2018**, *2*, 333. [CrossRef]
78. Chapman, B.; McDonald, K.; Shimada, M.; Rosenqvist, A.; Schroeder, R.; Hess, L. Mapping Regional Inundation with Spaceborne L-Band SAR. *Remote Sens.* **2015**, *7*, 5440–5470. [CrossRef]
79. US Census Bureau. Population Density by County: 2010. Available online: https://www.census.gov/library/visualizations/2010/geo/population-density-county-2010.html (accessed on 10 August 2020).
80. Yung, A.C.; Garcia, A.J. The October 1994 flood of Harris County, Texas. In *From the Mountains to the Sea-Developing Local Capabilities, Proceedings of the Nineteenth Annual Conference of the Association of State Floodplain Managers*; Portland, OR, USA, 22–26 May 1995; p. 3; Natural Hazards Research and Applications Information Center, University of Colorado: Boulder, CO, USA, 1995.
81. Cheng, X.; Pinto, N.; Gong, J. Terrain radiometric calibration of airborne UAVSAR for forested area. *Geo-Spat. Inf. Sci.* **2012**, *15*, 229–240. [CrossRef]
82. Duan, D.; Wang, Y. An Improved Algorithm to Delineate Urban Targets with Model-Based Decomposition of PolSAR Data. *Remote Sens.* **2017**, *9*, 1037. [CrossRef]
83. NOAA. Hurricane Harvey: Emergency Response Imagery of the Surrounding Regions. 2017. Available online: https://storms.ngs.noaa.gov/storms/harvey/index.html#14/29.8092/-95.2037 (accessed on 18 June 2020).

84. Bass, R.A.D.; O'Connor, B.; Perotin, M. A Summary of Findings from FEMA's Mitigation Assessment Team Evaluation of Texas Coastal Communities Impacted by Hurricane Harvey. In *Forensic Engineering 2018*; American Society of Civil Engineers: Reston, VA, USA, 2018; pp. 833–845. [CrossRef]
85. Davlasheridze, M.; Atoba, K.O.; Brody, S.; Highfield, W.; Merrell, W.; Ebersole, B.; Purdue, A.; Gilmer, R.W. Economic impacts of storm surge and the cost-benefit analysis of a coastal spine as the surge mitigation strategy in Houston-Galveston area in the USA. *Mitig. Adapt. Strat. Glob. Chang.* **2019**, *24*, 329–354. [CrossRef]
86. Potter, L.B.; Hoque, N. Texas Population Projections, 2010 to 2050. Office of the State Demographer, 4. 2014. Available online: http://www.txenergypoverty.org/wp-content/uploads/2015/12/2014-11_ProjectionBrief.pdf (accessed on 9 September 2020).
87. Kreitler, C.W. Fault Control of Subsidence, Houston, Texasa. *Ground Water* **1977**, *15*, 203–214. [CrossRef]
88. DellaPenna, T.M.; Hoelscher, C.; Hill, L.; Al Mukaimi, M.E.; Knap, A. How tropical cyclone flooding caused erosion and dispersal of mercury-contaminated sediment in an urban estuary: The impact of Hurricane Harvey on Buffalo Bayou and the San Jacinto Estuary, Galveston Bay, USA. *Sci. Total Environ.* **2020**, *748*, 141226. [CrossRef]
89. Potok, A.J. *Study of the Relationship between Subsidence and Flooding*; IAHS Publication (International Association of Hydrological Sciences): Wallingford, UK, 1991; pp. 389–395.
90. Warren, J.P.; Jones, L.L.; Lacewell, R.D.; Griffin, W.L. External Costs of Land Subsidence Houston-Baytown Area. *Am. J. Agric. Econ.* **1975**, *57*, 450–455. [CrossRef]
91. Al Mukaimi, M.E.; DellaPenna, T.M.; Williams, J.R. Enhanced land subsidence in Galveston Bay, Texas: Interaction between sediment accumulation rates and relative sea level rise. *Estuarine Coast. Shelf Sci.* **2018**, *207*, 183–193. [CrossRef]
92. Dixon, T.H.; Amelung, F.; Ferretti, A.; Novali, F.; Rocca, F.; Dokka, R.; Sella, G.; Kim, S.-W.; Wdowinski, S.; Whitman, D. Subsidence and flooding in New Orleans. *Nat. Cell Biol.* **2006**, *441*, 587–588. [CrossRef] [PubMed]
93. Kearns, T.J.; Wang, G.; Bao, Y.; Jiang, J.; Lee, D. Current Land Subsidence and Groundwater Level Changes in the Houston Metropolitan Area (2005–2012). *J. Surv. Eng.* **2015**, *141*, 05015002. [CrossRef]